



Lawrence Berkeley Laboratory

UNIVERSITY OF CALIFORNIA

Materials & Molecular Research Division

Submitted to Scripta Metallurgica

FERRITE STRUCTURE AND MECHANICAL PROPERTIES
OF LOW ALLOY DUPLEX STEELS

R.H. Hoel and G. Thomas

April 1981

TWO-WEEK LOAN COPY

This is a Library Circulating Copy
which may be borrowed for two weeks.
For a personal retention copy, call
Tech. Info. Division, Ext. 6782



LBL-11101
c.2

DISCLAIMER

This document was prepared as an account of work sponsored by the United States Government. While this document is believed to contain correct information, neither the United States Government nor any agency thereof, nor the Regents of the University of California, nor any of their employees, makes any warranty, express or implied, or assumes any legal responsibility for the accuracy, completeness, or usefulness of any information, apparatus, product, or process disclosed, or represents that its use would not infringe privately owned rights. Reference herein to any specific commercial product, process, or service by its trade name, trademark, manufacturer, or otherwise, does not necessarily constitute or imply its endorsement, recommendation, or favoring by the United States Government or any agency thereof, or the Regents of the University of California. The views and opinions of authors expressed herein do not necessarily state or reflect those of the United States Government or any agency thereof or the Regents of the University of California.

Ferrite Structure and Mechanical Properties of Low Alloy Duplex Steels

R. H. Hoel and G. Thomas

Materials and Molecular Research Division
Lawrence Berkeley Laboratory and Department of Materials
Science and Mineral Engineering,
University of California, Berkeley, California 94720

INTRODUCTION

Dual phase steels consisting of strong load carrying martensite in a ductile ferrite matrix form a relatively new class of strong, ductile steels for applications requiring tensile strengths of the order of 700 MPa ($1\text{MPa} = 10^6\text{Nm}^{-2}$, divide by 6.90 to convert to ksi). The mechanical properties are optimized by controlling the composite morphology, the volume fraction of martensite, the carbon content of martensite and the addition of different ternary and quaternary alloying elements, as summarized in recent symposia^{1,2}: It is generally accepted that the ultimate tensile strength of the dual phase aggregate will increase with the martensitic volume fraction V_m . Experimentally it has been shown that the tensile strength increases linearly with the martensitic volume⁴⁻⁹ and is given empirically by the law of mixtures

$$\sigma = \sigma_m V_m + \sigma_f (1 - V_m) \quad (1)$$

where σ_m and σ_f are the tensile strengths of respectively the martensite and ferrite phases. Normally, the yield strength is also found to increase with V_m . However, recent studies^{3,1} have shown that some dual phase steels show an unusual decrease in yield strength as the martensitic volume fraction increases. Figure 1 shows such a decrease in dual phase steels of compositions Fe|1.5Si|0.15C|0.03Nb (base + Nb) and Fe|1.5Si|0.15C|0.38Mo (base + Mo). These are all weight percent, unless otherwise is specified.

Thomas and Koo¹ suggested that the reason for the unexpected decrease in yield strength is as follows. The yield strength of the dual phase aggregate is primarily depending on the yield strength of the ferrite phase when this phase forms a continuous matrix with a fine dispersion of martensite islands. This assumption depends on the martensitic volume fraction not being too high. Furthermore, that since the carbide forming elements Nb and Mo are present, the ferrite phase is subject to precipitation strengthening. The level of this precipitation strengthening in the ferrite phase will decrease as the martensitic volume fraction increases, leading to an overall decrease in the yield strength of the dual phase aggregate.

The purpose of this communication is threefold. 1) To confirm the presence of and to characterize the precipitates in the ferrite phase of the base + Nb and base + Mo steels, 2) to study any possible variation in precipitate density as the martensitic volume fraction is changed and 3) to determine the level of precipitation strengthening.

EXPERIMENTAL

The dual phase steels described in this paper were all vacuum melted. The dual phase heat treatment consisted of austenitization at 1100°C, followed by intermediate quenching into an ice brine, annealing in the two-phase field, a final ice brine quench, and aging at room temperature for a few weeks.

In order to study the possible variations in precipitate density with martensitic volume fractions, it was necessary to measure foil thicknesses with an accuracy of a few percent. The most suitable method was found to be that of convergent beam microdiffraction^{14,15,16}. A brief description

and an example of such a measurement is presented in the appendix.

As basis for the determination of the precipitation strengthening level is used the classical Orowan mechanism. Orowan¹⁰ described the mechanism by which dislocations encounter and bypass point obstacles. The flow stress, τ , required to bypass such an obstacle is given by $\tau = \tau_0 + \alpha \frac{Gb}{\lambda_g}$, where τ_0 = flow stress of the ferrite in the absence of point obstacles, α = a geometrical factor depending on particle shape and distribution, G = shear modulus, b = Burgers vector of the glide dislocations, and λ_g = average spacing between obstacles in the glide planes. If the obstacles are spaced at distances less than the mean free dislocation slip length, an enhanced strengthening of the matrix occurs. In a metallic matrix the dislocation slip length is typically 1 - 50 μm .

RESULTS AND DISCUSSION

The presence of fine homogeneously nucleated precipitates in the ferrite matrix is evidenced in Figure 2. The matrix is oriented along the [001] zone axis. Upon tilting away from this orientation, some precipitates give rise to dislocation loop contrast, depending on their orientation relative to the direction of the electron beam (Figure 3). This is typical of coherent or partially coherent plate precipitates¹⁷. In figure 2 these plates are seen edge-on and they are oriented on or within 12° of the {100} planes. The plates oriented face on are invisible as $\underline{g} \cdot \underline{b} = 0$ and no strain contrast is observed in the surrounding matrix.

Weak beam imaging^{11,12} reveal plate thicknesses of less than 2.5nm and plate diameters ranging from 4nm to 25nm. The mean plate diameter is 13.5 (± 2)nm. Figure 3 shows examples of loops changing from outside

contrast to inside contrast as the sign of (g.b)s is reversed. The inside-outside contrast analysis¹³ of these precipitates show that they give rise to vacancy type loops which has been predicted for the early stages of precipitate formation¹⁸. These characteristic plate precipitates are common to both the base + Mo and base + Nb alloy systems.

Thin foils of the base + Nb alloy prepared within a few hours of heat treatment showed the presence of the same characteristic precipitates when examined in the electron microscope. Hence the precipitates are not formed as a result of room temperature aging. Upon tempering at 100°C for 1/2 hour no precipitate growth was observed. The size and morphology also remained unchanged as the tempering temperature was raised to 190°C and the time increased to 50 minutes. A similar sequence of tempering of an Fe|2Si|0.1C alloy, a composition similar to the base of the alloys described above, showed that upon tempering at 100°C for 1/2 hour some carbides start to coarsen. Tempering at 170°C for 1 hour¹⁹ and 200°C for 1 hour²⁰ results in a much more pronounced coarsening, and the presence of cementite precipitates ~17nm wide and 150nm long, has been reported²⁰. The increase in tempering resistance of the base + Nb alloy must be attributed to the presence of the niobium.

For precipitate density determinations, thicknesses were measured typically within an area of 100nm to 200nm in diameter (although better spatial resolution is possible) with an estimated accuracy of a few percent. The number of precipitates was counted from photographic prints within a typical true cross-sectional area of a few 10nm². The effect of particle overlap on the projected image could be ignored without introducing serious errors in the final result, and the effect of particles cut by

the foil surfaces was corrected for by the equation²¹.

$$N_A = N_V (x + 2r) \quad (3)$$

where N_A is the number of particles per unit projected area in a foil of thickness x , N_V is the particle density and $2r$ is the mean particle diameter. $2r$ is taken to be the diameter of an imaginary spherical precipitate whose volume is equal to that of an average sized plate precipitate of diameter D and thickness t . The value obtained for $2r$ is 7.3nm. The linear particle density, N_L , is calculated as the cube root of N_V and the mean distance between the centers of neighboring precipitates, ℓ , is taken as the reciprocal of N_L . Such distances were determined typically with an accuracy of $\pm 4\%$.

TABLE 1

Precipitate density, N_V , and mean interparticle distance, ℓ , as a function of composition and martensitic volume fraction, V_m

Composition	V_m , %	N_V , $\times 10^{14} \text{ cm}^{-3}$	ℓ , nm
Base + 0.03% Nb	20	81 ± 15	49.8 ± 3
Base + 0.03% Nb	40	38 ± 6	64.1 ± 3.5
Base + 0.03% Nb Tempered, 100°C, 1/2 hr.	20	85 ± 15	49.0 ± 2.7
Base + 0.38% Mo	20	77 ± 16	50.6 ± 3.5

Table 1 shows that as the martensitic volume fraction of the base + Nb alloy is increased from 20% to 40% there is an unmistakable decrease in precipitate density. The respective mean interparticle distance increases from 49.8 (± 3)nm to 64.1 (± 3.5)nm. The uncertainties quoted represent the limits of reproducibility from six independent measurements. Such limits are typically $\pm 6\%$. The absence of precipitate growth as this

alloy is tempered at 100°C is confirmed by measurement of the particle density which, within experimental error, is the same as that of the untempered material. Table 1 also shows that the precipitation density of the base + Mo alloy with a martensitic volume fraction of 20% is the same as that of the base + Nb alloy.

The validity of applying the Orowan model in calculating the level of precipitation strengthening is justified since for these alloy carbides it has been calculated that they will act as impenetrable barriers to dislocation motion²². The dispersion strengthening term, $\propto \frac{b}{\lambda g}$, in the Orowan equation (eqn. 1) has been modified by various authors (see²³ for a review) to take into account the finite particle size, more refined estimates of the dislocation line tension, the mutual interaction of the two bowed out arms of the dislocation on either side of the particle, and finally the particle shape. For plate (or rod) shaped particles of diameter D and thickness (or rod length) t the following expression has been derived for the dispersion strengthening, τ_D ,

$$\tau_D = \frac{0.83 Gb}{2\pi(1-\nu)^{1/2}} \times \frac{L+t}{L^2} \ln\left(\frac{D}{r_0}\right) \quad (5)$$

where ν is poisson's ratio, L is the effective interparticle distance (see below) and r_0 is the dislocation core radius. Calculations based upon an equation of this type have shown that thin plates can exert a strengthening influence up to 3 times greater than the same number of spherical particles of equivalent volume.

The equation derived by Fullman²⁴ for the effective particle spacing is $L = (tD/f)^{1/2}$, where f is the particle volume fraction. By definition $f = r^2/(\lambda/2)^2$, where r is the mean particle radius.

Equation 5 was used to estimate the magnitude of the precipitation strengthening levels of the base + Nb alloy, assuming the following values: $G = 79.8$ MPa, $b = 0.248$ nm, $\nu = 0.29$, $t = 1.4 (\pm 1.1)$ nm, $D = 13.5 (\pm 2)$ nm and $r_0 = 1.1 (\pm 0.3)$ nm. The values for ℓ are listed in Table 1. Assuming these values the level of precipitation strengthening with a martensitic volume fraction of 20% is $\tau_{20} = 274$ MPa. As V_m is increased to 40% the strengthening level drops to $\tau_{40} = 211$ MPa. It is the change in the precipitation strengthening level, $\Delta\tau = \tau_{20} - \tau_{40}$, that is of particular interest here. Inserting the uncertainties quoted above into equation 5 shows that the decrease $\Delta\tau = 71.8 (\pm 27)$ MPa.

With reference to Figure 1 and reference (3) it is seen that the observed decrease in the yield strength of the dual phase ferrite-martensite aggregate is 51.2 MPa as the martensitic volume fraction increases from 20% to 40%.

Let us consider an imaginary base + Nb alloy which in every way is identical to the experimental one described above, except that the ferrite phase is precipitate free and it shows the usual increase in yield strength as V_m increases. The above calculations show that the unexpected drop in the yield strength can be explained as a result of a reduced level of precipitate strengthening in the ferrite phase.

SUMMARY

It has been shown that previously unreported fine plate precipitates may be present in the ferrite phase of dual phase steels. The plates are oriented on the $\{100\}$ planes and in the Fe|1.5 Si|0.15 SC|0.03 Nb and Fe|1.5 Si|0.15 C|0.38 Mo alloys they significantly strengthen the ferrite phase. Based upon existing theories for precipitation strengthening, it

has also been shown that there is a significant drop in the level of precipitation strengthening as the martensitic volume fraction, V_m , increases from 20% to 40%. The corresponding drop in the observed yield strength of the dual phase aggregate supports the assumption that for a martensitic volume fraction up to 40% the yield strength of this aggregate is dominated by the yield strength of the ferrite phase.

Koo and Thomas^{1,2} have pointed out that the carbon content of the martensite decreases as V_m increases. It is well-established that the strength of this phase is proportional to its carbon content²². Hence the strength of the martensite will also decrease as V_m increases. Is therefore important to take the variations of σ_m and α_γ , with martensitic volume fraction, into account when applying the law of mixtures (equ. 1) to the ultimate tensile strength of dual phase steels.

ACKNOWLEDGEMENTS

The authors wish to thank Drs. U. Dahmen, R. Fisher and J. Y. Koo for helpful discussions and advice during this work. The work was supported by the National Science Foundation (R.H. Hoel), DMR 77-19358, Office of Energy Research, Office of Basic Energy Sciences, Materials Science Division of the U.S. Department of Energy under contract No. W-7405-ENG-48.

REFERENCES

1. G. Thomas and J. Y. Koo, Proceedings of the Symposium on Structure and Properties of Dual-Phase Steels, R. A. Kot and J. W. Morris, Eds., p. 183, The Met. Society of AIME, Warrendale, PA, (1979).
2. J. Y. Koo and G. Thomas, Proceedings of the Symposium on Formable HSLA and Dual Phase Steels, A. T. Davenport, ed., p. 40, The Met. Society of AIME, Warrendale, PA (1979).
3. P. K. Costello, Lawrence Berkeley Laboratory Report No. 8628 and M. S. Thesis, University of California, CA (1978).
4. B. Karlsson and G. Linden, Material Science Engineering 17, 209 (1975).
5. J. Y. Koo and G. Thomas, Met. Trans. A 8A, 525 (1977).
6. R. G. Davies, Met. Trans. A 9A, 41 (1978).
7. S. Hayami and T. Furukawa, Proceedings of the Symposium of HSLA Steels, J. Crane, ed., p. 311, Union Carbide Corporation, New York, (1975).
8. L. F. Ramos, D. K. Matlock and G. Krauss, Met. Trans. A 10A, 259 (1979).
9. J. Y. Koo, M. J. Young and G. Thomas, Met. Trans. A 11A, 852 (1980).
10. E. Orowan, Nature 149, 643 (1942).
11. D. J. H. Cockayne, Naturf. 27A, 452 (1972).
12. G. Thomas and M. J. Goringe, Transmission Electron Microscopy of Materials, 1st. ed., p. 305, John Wiley and Sons, New York (1979).
13. H. Föll and M. Wilkins, Phys. Stat. Sol. 31A, 519 (1975).

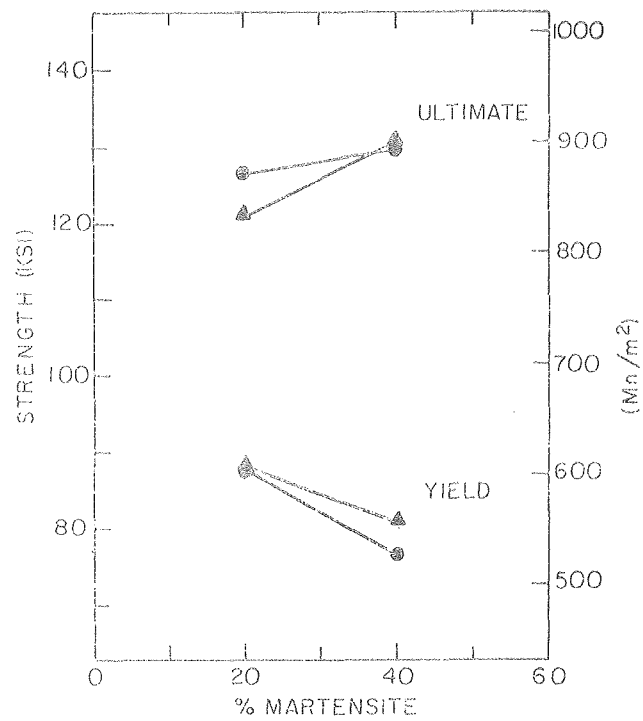
14. P. M. Kelly, A. Jostsons, R. G. Blake and J. G. Napier, Phys. Stat. Sol. 31A, 771 (1975).
15. T. Tan, W. L. Bell and G. Thomas, Phil. Mag. 24, 417 (1971).
16. S. M. Allen, Phil. Mag., in press.
17. G. Thomas and M. J. Goringe, "Transmission Electron Microscopy of Materials", 1st. ed., p. 159, John Wiley and Sons, New York (1979).
18. U. Dahmen, K. H. Westmacott and G. Thomas, Acta. Met., in press.
19. A. Pelton, Department of Materials Science and Mineral Engineering, University of California, Berkeley, CA, private communication.
20. J. Y. Koo and G. Thomas, Proceedings of the Symposium on Formable HSLA and Dual Phase Steels, A. T. Davenport, ed., p. 51, The Met. Soc. of AIME, Warrendale, PA (1979).
21. P. B. Hirsch, A. Howie, R. B. Nicholson, D. W. Pashley and M. J. Whelan, "Electron Microscopy of Thin Crystals", 2nd. ed., p. 424, Robert E. Krieger Publishing Company, New York (1977).
22. G. Thomas, D. Schmatz and W. W. Gerberich, Proceedings of the Second Berkeley International Materials Conference on High Strength Materials, V. F. Zackey, ed., p. 291, John Wiley and Sons, New York (1965).
23. P. M. Kelly, Int. Met. Rev. 18, 31 (1973).
24. R. L. Fullman, Trans. Amer. Inst. Min. Met. Eng. 197, 447 (1953).

FIGURE CAPTIONS

- Fig. 1 Shows the variation in ultimate tensile strengths and yield strengths of the base + 0.03 wt%Nb, ▲, and base + 0.38 wt%Mo, ●, alloys with martensitic volume fraction. Data from (3).
- Fig. 2 Shows the presence of fine homogeneously nucleated precipitates in the ferrite phase of the base + Nb alloy. This is also typical of the base + Mo alloy.
- Fig. 3 In certain orientations the precipitates show loop contrast. The encircled precipitates in figures a and b are examples of how the contrast changes from inside to outside as the sign of $(\underline{g} \cdot \underline{b})$ is reversed. The micrographs show precipitates in the base + Nb steel, but their appearance is identical to that of the Mo containing steels.
- Fig. 4 An example of thickness determination by convergent beam microdiffraction. The straight line intersects the ordinate in t^{-2} (t = thickness) and the slope equals ξ_g^{-2} (ξ_g = extinction distance).

APPENDIX

Figure 4 shows an example of a foil thickness measurement by two-beam convergent beam microdiffraction. The method involves plotting $s_i^2 |n_i|^2$ vs. $1/|n_i|^2$ where $s_i = \frac{\lambda}{d^2} \frac{\Delta\theta_i}{2\theta_d}$ and n_i is an integer. λ is the electron wavelength, d is the interplanar spacing of the observed reflection, $2\theta_d$ is the distance on the photographic print between the undiffracted disc, and $\Delta\theta_i$ is the distance from the center of the diffracted disc to the i th dark fringe. Such a plot will satisfy the equation $(s_i |n_i|)^2 + 1/\xi_g^2 |n_i|^2 = t^{-2}$, for the correct choice of n_i . A similar equation holds for the bright fringes¹⁶, and it is important to include these fringes in the measurement as they will compensate for any possible systematic error in the final result. As illustrated in Figure 4, a trial plot with different n_i values is made and a straight line is only obtained for the correct value. The straight line intersects the ordinate in t^{-2} . The slope is given by ξ_g^{-2} and provides a good check for the validity of the technique used. Linear regression and trend analysis is used to fit the best values to t and ξ_g . For the Nb containing steel described in the text and the reflection used in Figure 4, the experimental extinction distance is within 2% of the theoretical value for pure iron.



XBL 806-10321

Fig. 1

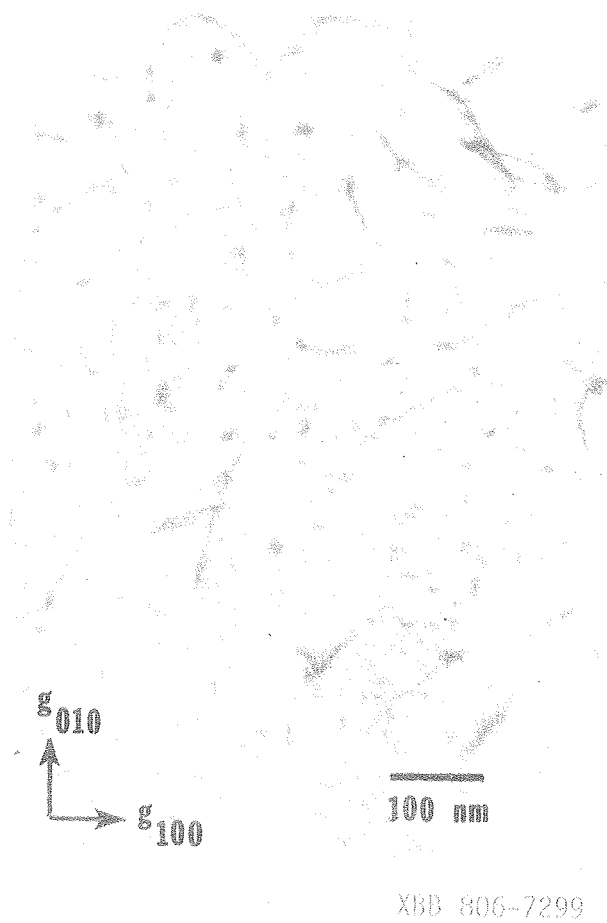
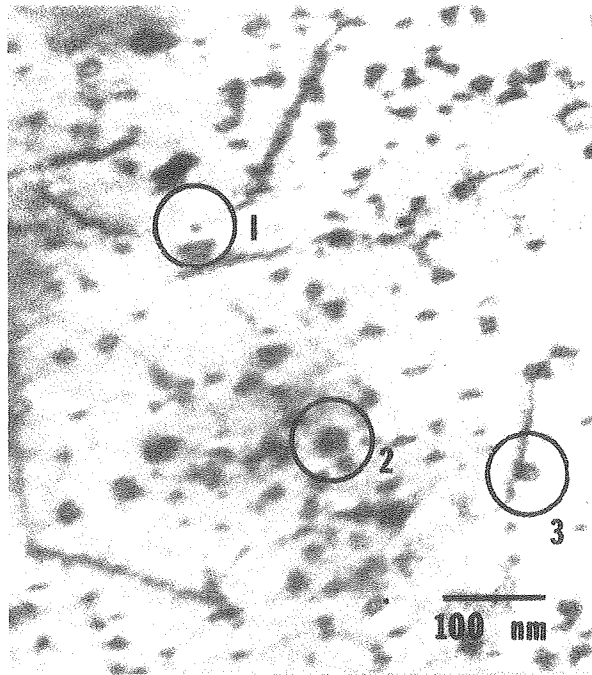
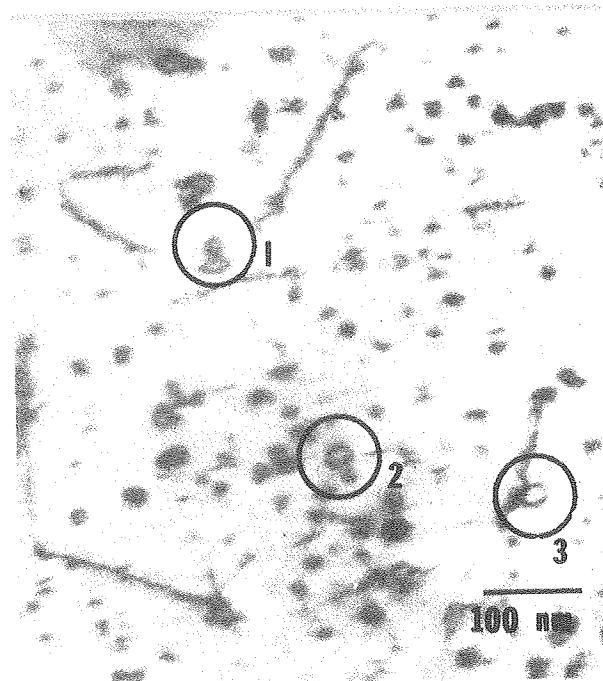


Fig. 2



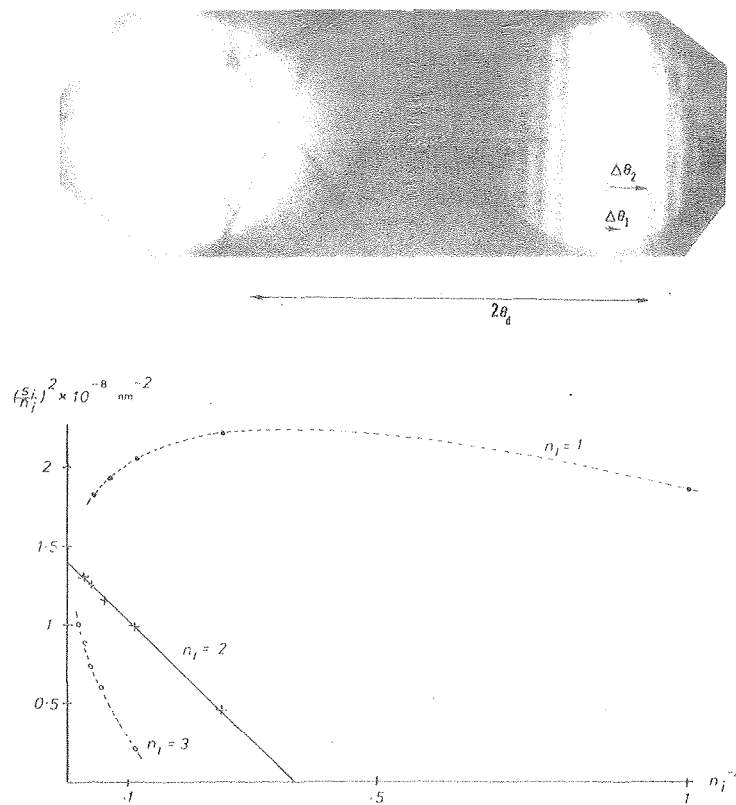
a



b

XBB 806-7296

Fig. 3



XBB 802-14490

Fig. 4